A FULLY IDENTIFIED SAMPLE OF AEGIS20 MICROJANSKY RADIO SOURCES

S. P. WILLNER[1], M. L. N. ASHBY[1], P. BARMBY[2], S. C. CHAPMAN[3], A. L. COIL[4], M. C. COOPER[5],
J.-S. HUANG[1], R. IVISON[6,7], AND D. C. KOO[8]

[1] Harvard-Smithsonian Center for Astrophysics, 60 Garden Street, Cambridge, MA 02138, USA
[2] Department of Physics & Astronomy, University of Western Ontario, London, ON N6A 3K7, Canada
[3] Institute of Astronomy, University of Cambridge, Madingley Road, Cambridge CB3 0HA, UK
[4] Department of Physics, University of California at San Diego, 9500 Gilman Drive, La Jolla, CA 92093, USA
[5] Department of Physics & Astronomy, University of California, Irvine, 4129 Reines Hall, Irvine, CA 92697, USA
[6] Astronomy Technology Centre, Royal Observatory, Blackford Hill, Edinburgh EH9 3HJ, UK
[7] Institute for Astronomy, University of Edinburgh, Blackford Hill, Edinburgh EH9 3HJ, UK
[8] UCO/Lick Observatory, Department of Astronomy & Astrophysics, University of California, Santa Cruz, CA 95064, USA

ABSTRACT

Infrared 3.6–8 μm images of the Extended Groth Strip yield plausible counterpart identifications for all but one of 510 radio sources in the AEGIS20 $S(1.4\,\mathrm{GHz}) > 50\,\mu$Jy sample. This is the first such deep sample that has been effectively 100% identified. Achieving the same identification rate at R band would require observations reaching $R_{\mathrm{AB}} > 27$. Spectroscopic redshifts are available for 46% of the sample and photometric redshifts for an additional 47%. Almost all of the sources with 3.6 μm AB magnitudes brighter than 19 have spectroscopic redshifts $z < 1.1$, while fainter objects predominantly have photometric redshifts with $1 \lesssim z \lesssim 3$. Unlike more powerful radio sources that are hosted by galaxies having large stellar masses within a relatively narrow range, the AEGIS20 counterparts have stellar masses spanning more than a factor of 10 at $z \sim 1$. The sources are roughly 10%–15% starbursts at $z \lesssim 0.5$ and 20%–25% active galactic nuclei mostly at $z > 1$ with the remainder of uncertain nature.

Key words: galaxies: active – galaxies: high-redshift – galaxies: photometry – infrared: galaxies – radio continuum: galaxies

Online-only material: color figures, machine-readable tables

1. INTRODUCTION

Radio observations are an excellent way to identify star-forming galaxies and active galactic nuclei (AGNs). Radio surveys are not subject to selection effects of obscuration or spectral line contamination, which affect visible-light surveys. Even very distant objects can have large radio flux densities. However, radio surveys alone are not sufficient to understand the populations, and follow-up observations are often more difficult than the initial radio survey. The problem is that redshift $z > 1$ sources are faint in visible light and require very deep follow-up studies in order to achieve identifications.

Despite the difficulties of counterpart identification, there are now several radio samples with identification rates of $\gtrsim$90%. Waddington et al. (2000) found optical counterparts for 96% of the sources in an $S(1.4\,\mathrm{GHz}) > 1$ mJy sample with images reaching $R = 26$. Ciliegi et al. (2003) found counterparts for 92% of $S(6\,\mathrm{cm}) > 50\,\mu$Jy sources with $I_{\mathrm{AB}} = 25$ images. Afonso et al. (2006) were able to identify only 89% of an $S(1.4\,\mathrm{GHz}) > 61\,\mu$Jy radio sample even with *Hubble Space Telescope* (*HST*)/Advanced Camera for Surveys observations reaching magnitude $z_{850} = 28$. Simpson et al. (2006) identified >90% of a 100 μJy radio sample using $BRi'z'$ images reaching AB magnitude 27. Mainieri et al. (2008), using data over a wide wavelength range including the infrared, chose counterparts for 95% of a 42–125 μJy radio sample but with an estimated 3% rate of spurious identifications. In other recent work, Bardelli et al. (2010) reported an 82% identification rate in an $\sim$50 μJy radio sample in the COSMOS field, and Afonso et al. (2011) achieved 83% identification of a sample of ultra-steep-spectrum radio sources with $S(610\,\mathrm{MHz}) > 100\,\mu$Jy in the Lockman Hole. Huynh et al. (2008) identified 79% of a much fainter

($S(1.4\,\mathrm{GHz}) > 10\,\mu$Jy) radio sample using deep *HST* images ($I_{\mathrm{AB}} < 26$), albeit with a relatively large matching radius (up to 1$''$96).

Even when counterparts are detected, observed visible light corresponds to rest-frame ultraviolet for high-redshift galaxies. While this can give a measure of star formation *rate*, it gives little indication of stellar *mass* and thus little indication of the type of galaxy hosting the radio source. Radio-quiet AGNs and star-forming galaxies both contribute to the faint radio population, but lack of complete identifications and limited wavelength coverage make the proportions uncertain (e.g., Huynh et al. 2008).

The All-wavelength Extended Groth strip International Survey (AEGIS; Davis et al. 2007) offers an unprecedented combination of deep, multiwavelength data over a large area, the Extended Groth Strip (EGS). The data include a radio survey at 20 cm, AEGIS20 (Ivison et al. 2007), which reaches a sensitivity limit of 50 μJy beam^{-1}. Willner et al. (2006) showed that infrared observations of radio sources can produce very high identification rates for radio source counterparts, albeit at much higher flux densities (55 mJy beam^{-1}) than AEGIS20 and at 6 cm rather than 20 cm. Park et al. (2008) claimed to find all the AEGIS20 radio sources that are also 24 μm sources on the IRAC images but used a 2$''$5 matching radius. IRAC data at a 20 minute depth contributed to the Afonso et al. (2011) identifications in the Lockman Hole. Infrared data should give high identification rates because the SED of typical stellar populations peaks near 1.6 μm. For a distant source, this peak will be redshifted to longer wavelength, and the IRAC 3.6 and 4.5 μm flux densities will not decrease as rapidly as might be expected. Passive evolution also increases the observed flux densities in these bands: a stellar population of a given mass was brighter
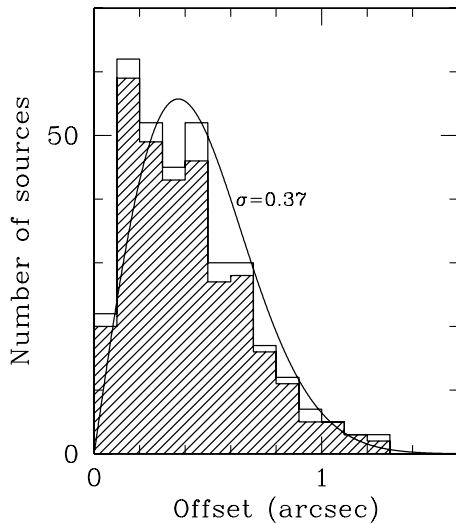
Figure 1. Histogram of radial offsets between radio and IRAC positions for 340 radio point sources. The shaded region shows offsets for 314 sources with [3.6] < 22. The curve shows the expected distribution for Gaussian position errors of $0\farcs37$ (Barmby et al. 2008) in each coordinate.

Table 1
20 cm Radio Sources with IRAC Coverage

ID	AEGIS20	Flux Density (mJy)				Size ($''$)		P.A.
		Peak	Unc[a]	Int	Unc[a]	Major	Minor[b]	(deg)
1	J141758.05+523134.5	0.161	0.028	0.161	0.028	0.0	0.0	0.0
2	J141736.35+523135.8	0.490	0.029	2.222	0.158	9.4	5.2	92.9
3	J141732.61+523203.3	0.850	0.032	0.910	0.057	1.7	0.0	120.6
4	J141809.94+523300.2	2.684	0.023	2.829	0.042	1.2	0.5	172.9
5	J141754.89+523307.1	0.152	0.027	0.152	0.027	0.0	0.0	0.0

Notes.
[a] Tabulated uncertainties in flux density are 1σ. Values of -1 in integrated uncertainty indicate that the source was poorly fitted by a Gaussian. In these cases, integrated flux density was measured in a polygon that included the entire source, and minor axis sizes are not given.
[b] A value of -1 in the Minor Size column indicates a radio source well fit by a pair of Gaussians. In these cases, Major Size is the separation between components.

(This table is available in its entirety in a machine-readable form in the online journal. A portion is shown here for guidance regarding its form and content.)

in the past when it was younger. (See Figure 1 of Eisenhardt et al. 2008.) Thus, counterparts should be visible in IRAC observations unless they are either extremely distant, have very low mass, or are heavily obscured by dust, neither of the latter two being likely for a powerful radio galaxy.

This paper reports the matching of AEGIS20 radio sources primarily to IRAC 3.6–8.0 μm data. Barmby et al. (2008) have provided images and catalogs of IRAC data in the EGS. The typical exposure time is 2.5 hr (9 ks), and the 80% completeness limits for the catalog are $\sim$5 μJy at 3.6 and 4.5 μm and $\sim$10 μJy at 5.8 and 8.0 μm. However, fainter objects with known positions can be identified on the images. Additional IRAC data for the EGS exist (M. L. N. Ashby et al. 2012, in preparation) but were not used for this work. In practice, the Barmby et al. data suffice to identify counterparts for all or nearly all of the radio sources. The radio sample is defined and source matching is described in Section 2, counterpart properties including photometry and redshifts are given in Section 3, and results are discussed in Section 4 and summarized in Section 5. Throughout this paper, magnitudes are in the AB system, and the notation $[w]$ means the AB magnitude at wavelength w in μm.[9] Source distances are based on standard ΛCDM cosmology with $H_0 = 71$ km s^{-1} Mpc and $\Omega_M = 0.27$. Practical calculation of luminosity distances was based on the program ANGSIZ (Kayser et al. 1997).

2. SAMPLE DEFINITION AND IDENTIFICATIONS

2.1. Selecting Counterparts with IRAC Data

The initial radio catalog (Ivison et al. 2007) contains 1122 sources[10] with $S(1.4\,\text{GHz}) > 50\,\mu$Jy. Of these, 511 are in the area of IRAC coverage, defined by at least five independent images in each of the four IRAC channels. (This amounts to one-tenth the nominal IRAC exposure time, but most sources were observed with the nominal exposure time or close to it.) These 511 radio positions, within an area of $\sim$950 arcmin^2, are the ones we have attempted to match to IRAC sources.

The simplest radio sources to match were the point sources, those unresolved at the $3\farcs8$ FWHM of the radio beam (Ivison et al. 2007). There are 342 such sources in the input list. One is $3\farcs0$ from the bright ($K_S = 8.4$) star 2MASS J14230588+5333504. No identification is possible for this one, and it was dropped from further consideration. Of the remaining 341 sources, all but one coincide with an IRAC catalog source consistent with Gaussian position uncertainties having a standard deviation of $0\farcs37$ in each coordinate. There is no systematic offset in right ascension, and the offset in declination is $0\farcs08$, the IRAC positions being systematically north of the radio positions. Figure 1 shows a histogram of the radial offsets. The one badly discrepant source is 434 (Table 1), which has an offset of $1\farcs6$.[11] This is too large to be considered a valid identification, and if the radio source is real, then it remains unidentified. The radio flux density is at the catalog limit of 50 μJy, just under a 5σ detection. Thus, 340 of the 341 point sources possible to match are indeed matched by catalog IRAC sources.

Most of the resolved radio sources are equally simple to match—the sources are small, and there is an obvious IRAC counterpart—but some of the complex, resolved sources present more of a challenge. For seven radio sources, the IRAC data suggest two possible counterparts. Radio images for these seven are elongated and statistically consistent with two point sources separated by a few arcseconds. In four of these cases, detection of the weaker radio source was less than 3σ significance. In these cases, the radio source was deemed to be a single point source, and the nearest galaxy to it was adopted as the counterpart. The other galaxy might be a radio source as well, but its flux density is below the sensitivity limit of the AEGIS20 survey. In the other three cases, both radio components were detected at $>3\sigma$, and these are treated as separate sources, each radio component having an IRAC counterpart. Radio to IRAC offsets are consistent with the position uncertainties found for the point sources.

---

[9] Some other papers use the $[w]$ notation to mean Vega magnitudes, but here it means AB.
[10] One source in the original catalog is a duplicate.

[11] Other sources with large offsets are 033 and 487 with offsets of $1\farcs3$. The latter source is near the edge of the IRAC map and has only 1/10 normal coverage; its IRAC position uncertainty is thus expected to be about three times larger than normal. Indeed, a systematic shift is seen between the 3.6 and 4.5 μm images for this source. Source 33 has full-depth IRAC coverage with no obvious position error, but its offset could be the 3σ outlier expected in this sample. It is a 5.4σ radio detection, and thus unlikely to be spurious.
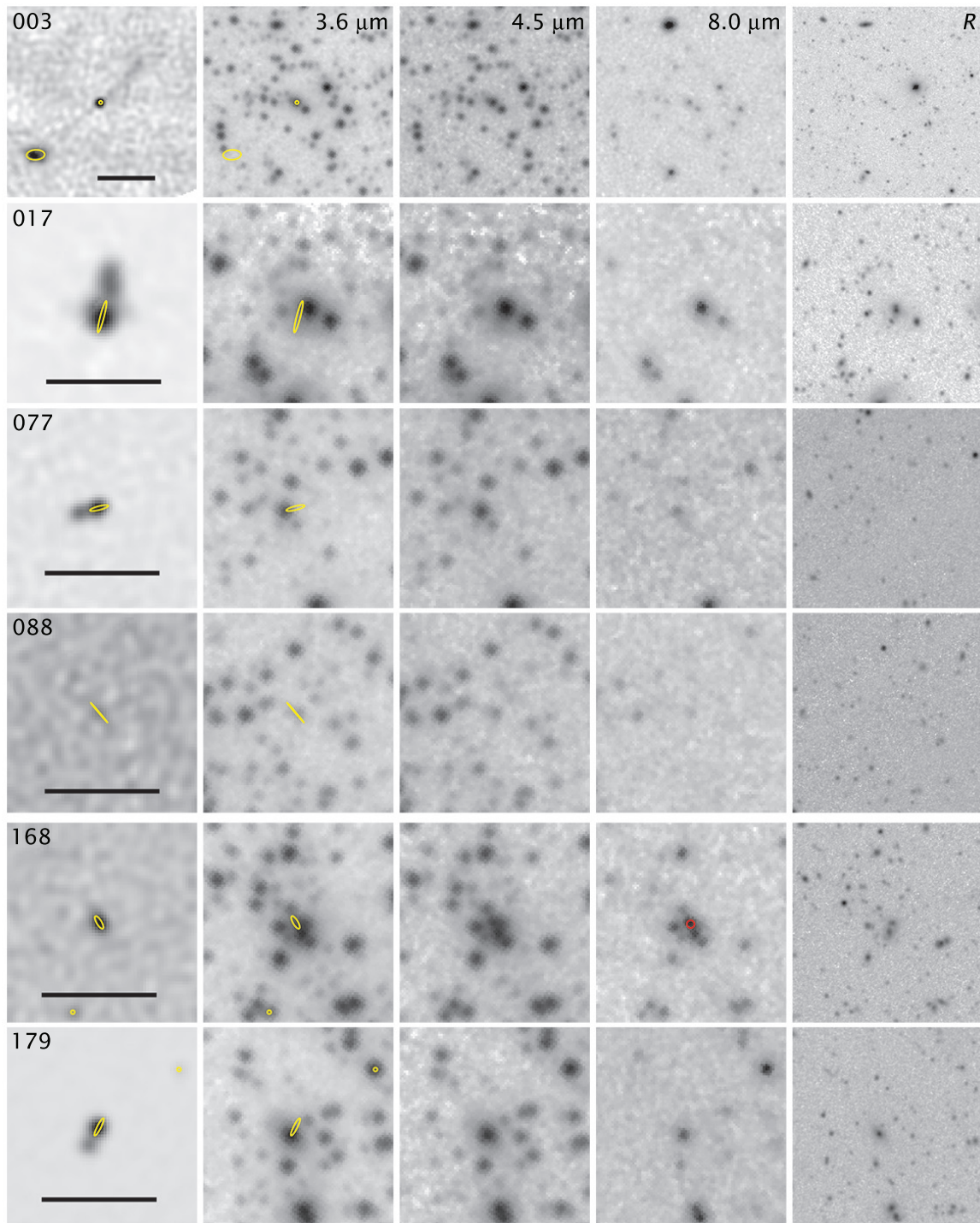
Figure 2. Postage stamp images of complex sources. From left to right, each row shows the VLA 20 cm radio, the IRAC 3.6 μm, 4.5 μm, and 8.0 μm images and the Subaru R image of a source. The source numbers from Table 1 are indicated in the left panels. Scale bars indicate 30''; each stamp image is 100'', 50'', or if no scale bar is shown, 25'' across. North is up and east to the left in all images. Yellow contours show the Gaussian fit (Ivison et al. 2007) to the deconvolved radio source. The fits are generally smaller than the radio images themselves because of the radio beam size. Red circles are 2'' in diameter and show the position of the IRAC counterpart where it might not be obvious.

(A color version of this figure is available in the online journal.)

Table 2
Radio Sources with No IRAC Identification

ID	AEGIS20	Comment
002	J141736.35+523135.8	Radio source is hot spot in jet from 003
434	J142213.25+532817.5	Radio source $<5\sigma$, nearest IRAC source 1''.6 away
488	J142306.17+533351.8	Near saturated star

3

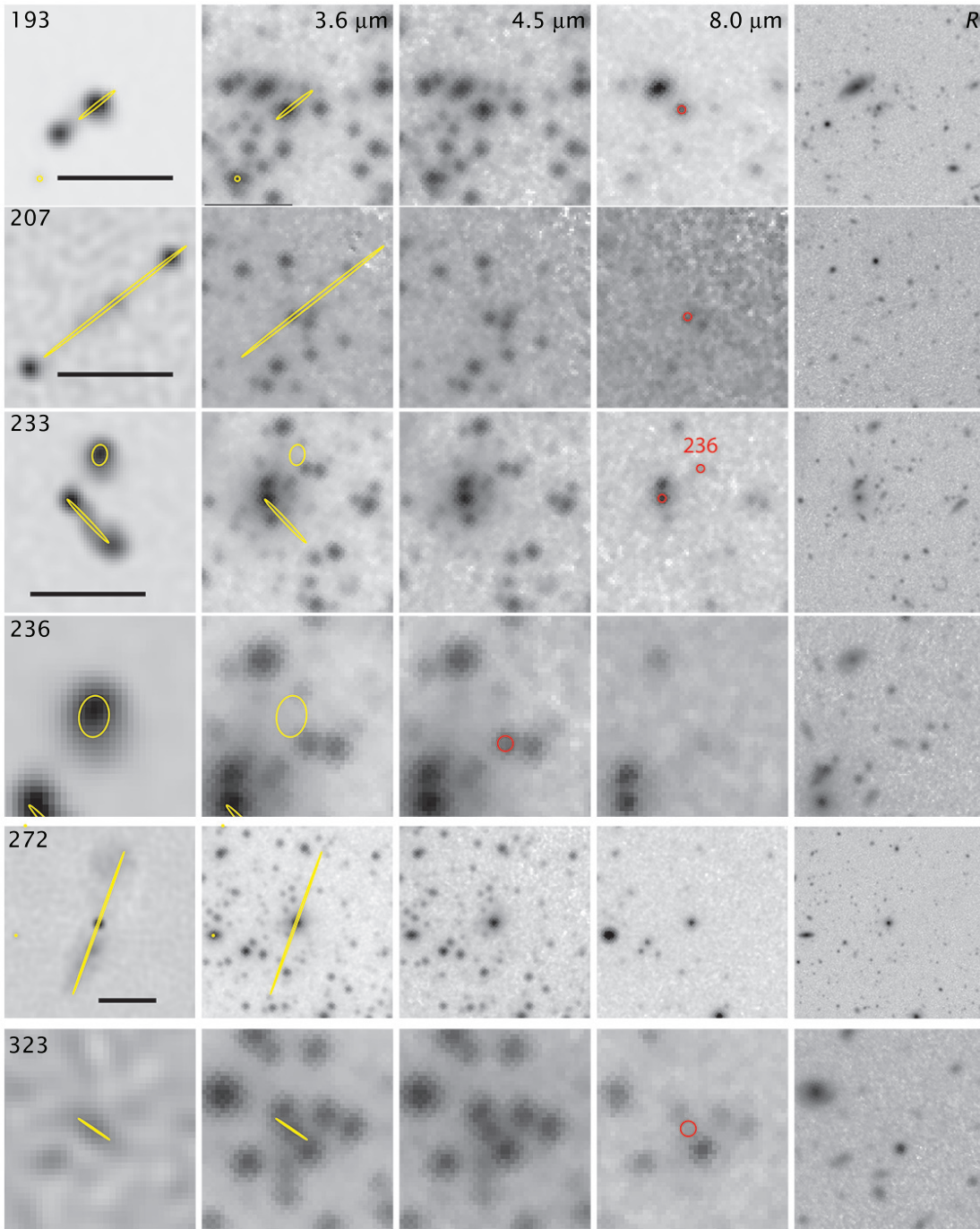193   3.6 μm   4.5 μm   8.0 μm   R

207

233   236

236

272

323

Figure 2. (Continued)

Finally, there are 15 radio sources with complex morphologies, as shown in Figure 2. All but one have a plausible IRAC counterpart, though in some cases there are multiple candidates, and there is no way to be certain we have chosen the correct one. For source 002, there is a bright IRAC source within $5\rlap{.}''5$ of the radio peak, but a more plausible explanation is that source 002 is the tip of a jet emerging from source 003. There is a counterjet in the opposite direction, though it is not bright enough in the radio image to have been detected by the automated search as a separate source. The extended ($\sim 5''$) radio source 236 is $4\rlap{.}''3$ from our suggested IRAC counterpart (an $R = 24.4$ galaxy at $z_{\rm phot} = 0.69$), corresponding to a projected separation of about 30 kpc. Alternative IRAC identifications are a fainter galaxy

(shown at the northern tip of the radio ellipse in Figure 2) $3\rlap{.}''4$ from the radio centroid[12] or that 236 is a radio lobe of source 233 to the southeast. Source 233 has a radio jet and lobe extending to its southwest, but the radio image shows no evidence of any jet connecting 233 to 236. Source 428 has multiple radio lobes, and the counterpart could be any of many sources visible in the IRAC image. We suggest that the most likely counterpart is a $z = 0.8260$, $R = 22.7$ galaxy bright at $8\,\mu$m and located near the inner edge of the northwest radio lobe. At the suggested redshift, the projected $42''$ maximum extent of the radio lobes corresponds to a length of 320 kpc. Table 2 lists the three radio

_____
[12] $R = 24.5$, $z_{\rm phot} = 0.6$ according to the Rainbow database.
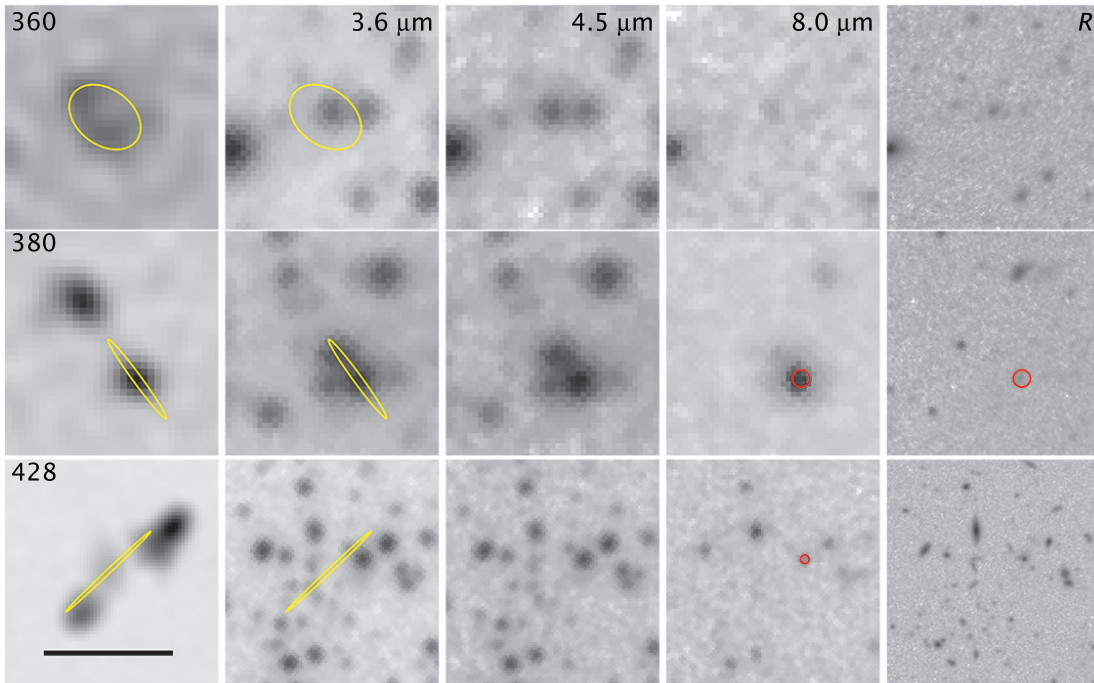
Figure 2. (Continued)

sources unmatched by IRAC counterparts, and Table 3 gives IRAC counterpart positions and other information for the radio sources that were matched.

The overall identification rate is remarkably high. At most, three of the 510 radio sources lack IRAC counterparts, and there is a plausible case that the identification rate is 100%. This would require source 2 to be a jet from 3 (as is likely), source 236 to be related to one of two candidate counterparts or be a jet from 233, and AEGIS20 radio source 434 to be spurious. At the near-5σ detection level, even a single spurious source is statistically unlikely, but the absence of an IRAC counterpart is hard to explain. At $z = 1$, the IRAC 3.6 μm detection limit 0.7 μJy[13] corresponds to a stellar luminosity of the order of $10^9\,L_\odot$, and such low-luminosity galaxies are unlikely to harbor powerful radio sources. Even at $z = 5$, a galaxy with $L = 10^{11}\,L_\odot$ should have been detected at 4.5 μm. Nevertheless, Huynh et al. (2010) reported two radio sources in the Extended *Chandra* Deep Field South without apparent IRAC counterparts. If such a population exists, then source 434 (and less likely source 236) could be a member. The source density suggested by Huynh et al. predicts >4 such sources in the EGS field, where we find at most two and maybe none. This implies that radio sources without IRAC counterparts are rare if they exist at all.

2.2. Selecting Counterparts with R-band Data

Deep Subaru *R*-band data exist for almost the entire EGS[14] with 5σ depths of 26.5 AB magnitudes over most of the strip and 26.1 in the southwest portion. These images were searched with SExtractor (Bertin & Arnouts 1996), and 405 counterparts were found within 1″ of the IRAC position. The number would be 372 if a more stringent (and more reasonable) coincidence criterion

<0″.7 were used.[15] This detection rate of <80% (or <73%) is typical of visible-light counterpart searches (Section 1). Moreover, for 10 radio sources, the automated *R* search found a neighbor object brighter in *R* instead of the object detected by IRAC. We regard the latter as more plausible counterparts because most radio sources originate in massive galaxies, which may be red but will seldom have very blue colors, as would be required if any of these 10 *R* sources is the correct counterpart. Therefore, about 2%–3% of the proposed counterparts would be incorrect in the 1″ search, though all of these would be eliminated with the 0″.7 search. Mainieri et al. (2008) also gave examples of counterparts found in the infrared K_s band or IRAC data but invisible at shorter wavelengths. Figure 3 shows images of some sources that an automated *R*-band search might misidentify.

3. COUNTERPART PROPERTIES

3.1. Source Photometry

No single method of photometry is adequate for all objects. With deep images, many radio counterparts have nearby sources that can contribute to the photometry in large apertures. Other counterparts are significantly extended, and only large apertures can capture all the flux. There are technical problems in some cases because an automated aperture selection can combine unrelated objects or separate a single object into multiple ones, though the latter does not seem to have occurred in the present sample. In practice, we have measured IRAC and *R*-band fluxes through four apertures for each object: three circular apertures

---

[13] This limit is for the nominal survey exposure time of 9 ks. The actual exposure time at the position of 434 was 3.4 ks at 3.6 μm and 6.6 ks at 4.5 μm, so the actual limits for this source are correspondingly worse.

[14] Five counterparts in the northern part of the EGS are outside the coverage of the *R* images.

[15] The search was based on IRAC positions because the purpose was to determine whether an apparent *R* counterpart was the same object as the IRAC source. A purely visible search for radio source counterparts would, of course, start from VLA positions rather than IRAC positions and would probably find slightly fewer counterparts than the numbers stated.
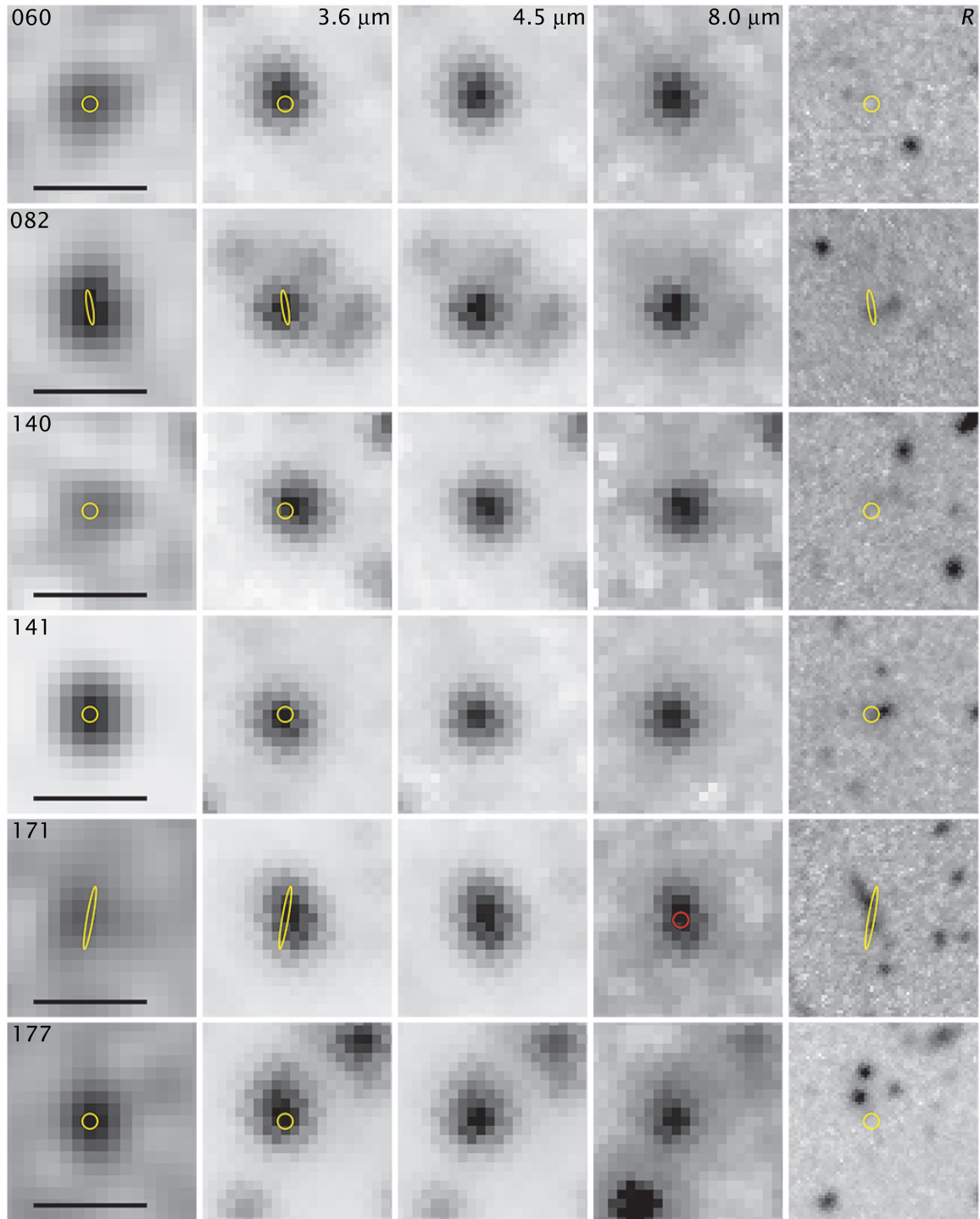
Figure 3. Postage stamp images of counterparts that might be misidentified if only *R* images were available and one source possibly lacking an IRAC counterpart. Each row shows one source with number (Table 1) indicated in the left panel. Panels from left to right show the 20 cm radio image, IRAC 3.6 μm, 4.5 μm, and 8.0 μm images, and the Subaru *R* image. Scale bars indicate 7″.5; each stamp image is 12″.5 across. North is up and east to the left in all images. Yellow contours show the Gaussian fit (Ivison et al. 2007) to the deconvolved radio source or a 1″ diameter circle if the radio source was unresolved. Red circles are 1″ in diameter and show the position(s) of the IRAC counterpart(s).

(A color version of this figure is available in the online journal.)

with radii 1″.53, 2″.14, and 3″.06[16] and the Kron aperture chosen by SExtractor (MAG_AUTO).

The default photometry aperture was the smallest circular one because of its rejection of neighboring sources and sky

---

[16] These aperture sizes were those used in the IRAC catalog (Barmby et al. 2008) and correspond to 2.5, 3.5, and 5.0 IRAC mosaic pixels. The IRAC mosaics have pixels half the size of the actual IRAC pixels.

fluctuations, but all galaxies with semimajor axis size >1″.22 (measured by SExtractor in *R*) were examined individually on the images, as were objects with $m(1″.53) - m(2″.14) > 0.25$ or $|m(3″.06) - m_{\rm auto}| > 0.25$. In each case, the most reasonable magnitude to include the whole galaxy but exclude neighbor objects was chosen. This process was necessarily somewhat subjective, but no alternative reasonable choice would
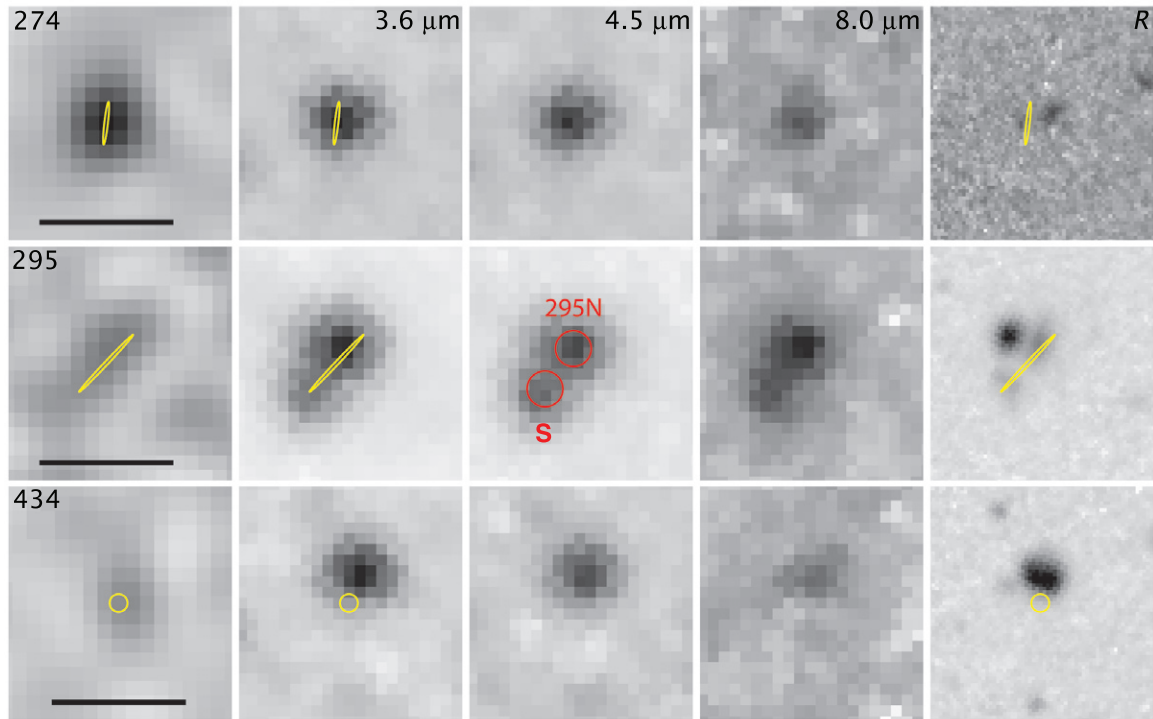
Figure 3. (Continued)

change the magnitude by more than about 0.2 mag. In all, 166 counterparts were examined individually to choose apertures.

SExtractor (Bertin & Arnouts 1996) was used to measure both circular and AUTO magnitudes for the sources it detected; the SExtractor IRAC magnitudes were published by Barmby et al. (2008).[17] For sources not detected by the automated SExtractor search, positions were measured from the images and aperture photometry done at those positions with the IRAF task apphot. The R magnitudes were calibrated from SDSS stars (avoiding those saturated in the Subaru data), for which $R_{\rm Subaru} = r_{\rm Sloan} + 0.17(r-i)_{\rm Sloan}$ with rms scatter $\sim$0.05 mag.[18] The R magnitudes are given in Table 4, and IRAC magnitudes are given in Table 5, which uses SExtractor magnitudes when they exist and apphot magnitudes otherwise. When AUTO magnitudes are used, the Kron apertures were derived separately in the IRAC bands and in R and may differ, but in both cases they are intended to measure the total magnitude of the object. The uncertainties listed in Tables 4 and 5 are statistical only as derived from the local background fluctuations. Upper limits are 5σ.

The R magnitudes were checked in two ways. The Subaru data came from three adjacent images, which overlap enough to include duplicate images of 26 sources not strongly affected by artifacts or image edges. The rms absolute difference of observations of the same source in the $1\rlap{.}''53$ aperture is 0.04 mag, and the maximum is 0.10 mag. However, a difference of 0.86 mag was found for one source near an image edge (one image being obviously bad at that location), and a very few

sources near image edges or with other problems might have bad magnitudes that have not been noticed. The rms difference between SExtractor and apphot $1\rlap{.}''53$ aperture magnitudes is 0.09 mag, presumably due to differences in aperture centering and background calculations. This is a reasonable lower limit on systematic uncertainty for the fainter sources. However, it seems prudent to recognize that in some cases the source measured in R may be a different object than the one measured by IRAC, and a few large errors are possible.

The new apphot IRAC aperture measurements agree with the published ones except when there are nearby, confusing sources. In some of those cases, SExtractor can separate the sources, whereas apphot simply adds all the counts in the defined aperture. Otherwise, testing showed that SExtractor and apphot magnitudes are consistent with each other. Barmby et al. (2008) discussed the uncertainties in the IRAC data, and the new measurements should have equivalent uncertainties. Figures 4 and 5 show the magnitude distributions of the radio source counterparts in [3.6] and R, respectively.

3.2. Source Redshifts

Spectroscopic redshifts come from a variety of sources. The largest number (125) are from the DEEP2 redshift survey (Davis et al. 2007; Newman et al. 2012). Additional redshift sources are listed in notes to Table 4. All in all, 235 counterparts have spectroscopic redshifts, and agreement is excellent for the 44 sources with more than one spectroscopic measurement.[19]

Barro et al. (2011a) have compiled a database of photometric and spectroscopic data[20] in the EGS and used it to derive photometric redshifts (Barro et al. 2011b). Searching their database using the IRAC positions (Table 3) of the radio source counterparts and eliminating duplicates resulted in 440 matches within

---

[17] Source 036 is not in the published catalog, but its AUTO magnitudes were measured on the images in the same way as for the catalog. Extended source corrections of 0.062, 0.040, 0.137, and 0.212, based on the latest coefficients from the *Spitzer* Science center, are included in the Table 5 magnitudes. The channel 2 correction differs by 0.016 mag from the one that would have been used in 2008, but 036 is the only radio source counterpart that needs an extended source correction.

[18] The color term is poorly determined because the $r-i$ color covers only the range 0–2 mag.

[19] $\Delta z \leqslant 0.0015$, except for one source with $\Delta z = 0.0054$.

[20] The Rainbow database can be found at https://rainbowx.fis.ucm.es/Rainbow_navigator_public/.

Table 3
IRAC Counterparts of EGS 20 cm Radio Sources

ID	R.A.	Decl.	EGSIRAC	Offset[a]	Exposure[b]	IRAC[c]	Offset[d]	Comment
001	214.49231	52.52630	J141758.15+523134.6	0.9	54	. . .	. . .	Companion 3.2″ NE
003	214.38602	52.53422	J141732.64+523203.1	0.3	56	166271	0.16	
004	214.54145	52.55013	J141809.94+523300.4	0.2	50	158078	0.04	
005	214.47884	52.55180	J141754.92+523306.4	0.7	58	160802_1	0.23	

Notes.
[a] Radial offset in arcsec from IRAC to radio position. Where a source name is shown, IRAC names and positions are from the published catalog (Barmby et al. 2008). For counterparts not in the published catalog, source positions were measured on the published images.
[b] Number of useful images in whichever IRAC wavelength has the fewest in units of 200 s (one image at 3.6–5.8 μm; 4 images at 8.0 μm; see Barmby et al. 2008).
[c] Source name in Rainbow database (Barro et al. 2011a).
[d] Radial offset in arcsec from IRAC position measured here to source position in Rainbow database.

 (This table is available in its entirety in a machine-readable form in the online journal. A portion is shown here for guidance regarding its form and content.)
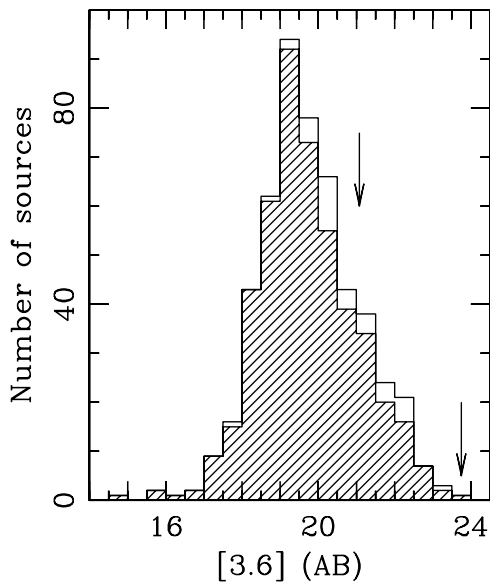

Figure 4. Histogram of 3.6 μm magnitudes of radio source counterparts. The hatched histogram shows magnitudes for sources with redshifts. Arrows show the 90% and 50% completeness limits of the Barmby et al. (2008) catalog, but magnitudes can be measured on the images to fainter limits than these. Bins are half a magnitude in width because the distribution of 3.6 μm magnitudes is narrower than the distribution of R magnitudes (Figure 5).
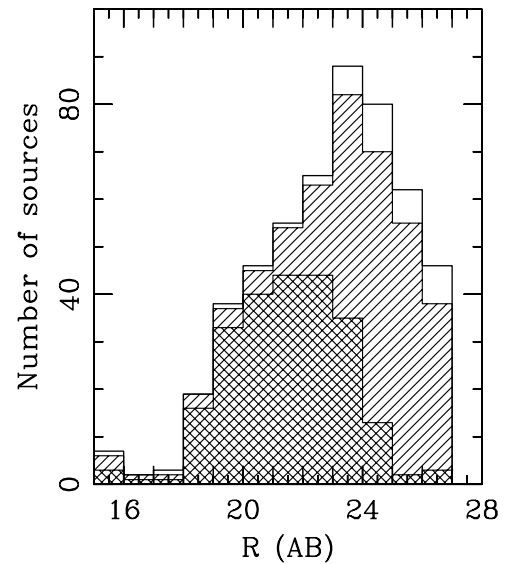

Figure 5. Histogram of R magnitudes of radio source counterparts. The hatched histogram shows magnitudes for sources with redshifts (including photometric ones), and the cross-hatched histogram for sources with spectroscopic redshifts. When no source was detected at R, its magnitude was placed in the bin corresponding to the upper limit. Some sources are likely much fainter than $R = 27$.

$0.''65$. We examined images and found eight additional cases where the Rainbow object appears to be the one we identify as the radio source counterpart; position offsets for these were between $0.''65$ and $0.''80$. No objects with offsets $>0.''8$ appeared to be valid matches. Of the 448 matched objects, 215 have spectroscopic redshifts, and all but 21 agree with the Barro et al. (2011b) photometric redshifts within $\Delta z \leqslant 0.2$. Another large source of photometric redshifts for the EGS is the CFHT Legacy Survey (CFHTLS; Coupon et al. 2009), with 183 altogether of which 105 are for objects with spectroscopic redshifts. Of these, 94 photometric redshifts are within $\Delta z \leqslant 0.2$ of the spectroscopic ones, again giving a success rate near 90%. The next largest source is the NEWFIRM Medium Band Survey (NMBS Whitaker et al. 2011) with 76 redshifts. Of these, 5 of 42 differ from a spectroscopic measurement by $\Delta z > 0.2$. Finally, 236 photometric redshifts are from unpublished work (Huang et al. 2012). These use a neural network technique that is inherently limited to $z \leqslant 1.1$ because of insufficient galaxies at larger

redshifts in the training set. Nevertheless, of 71 with spectroscopic measurements, only 11 deviate by more than $\Delta z = 0.2$. The overall results suggest a photometric redshift success rate near 90%, but sources lacking spectroscopic redshifts tend on average to be fainter, and the success rate could be lower for them. Table 4 gives the best redshift we could find for each object. We have preferred NMBS if available because the use of medium-band filters should give better redshift performance. The least-preferred survey was the one from Huang et al. (2012) because of its limitation to $z < 1.1$, but order of preference among the other surveys was not obvious. Changing the order would not change the results of this paper. All in all, Table 4 has 235 spectroscopic redshifts, 238 photometric redshifts, and 38 objects with no redshift available. Thus, about 93% of the radio source counterparts have a redshift of some kind, but at least 24 of the photometric redshifts (5% of the full sample) likely differ from the true redshift by $\Delta z > 0.2$.

Table 4
R Magnitudes and Redshifts of Radio Source Counterparts

ID	R.A.[a]	Decl.[a]	Offset[b]	Mag Type[c]	R	±[d]	z	z Source[e]	L(3 GHz)[f]
001	. . .	. . .	. . .	5	23.77	0.02	0.95	6	3.6E+23
003	214.38594	52.53426	0.23	1	23.13	0.01	0.9859	2	2.2E+24
004	214.54142	52.55020	0.28	1	25.14	0.09	2.87	6	7.9E+25
005	214.47884	52.55183	0.12	1	25.30	0.10	1.84	6	1.6E+24
006	214.59998	52.55628	0.43	1	23.35	0.02	1.20	6	6.5E+23

Notes.
[a] J2000 position of counterpart if measured independently on *R* image.
[b] Distance in arcseconds from *R* to IRAC position of counterpart.
[c] Magnitude type: 1–3 = SExtractor aperture magnitudes in $1''53$, $2''14$, or $3''06$ radii, respectively, 4 = magnitude in Kron aperture as measured by SExtractor, 5–7 = `apphot` magnitude with same aperture sizes as 1–3, respectively, measured at *R* position if available, otherwise IRAC position. Magnitudes are AB.
[d] Magnitude uncertainties given here are statistical only, estimated from sky fluctuations. See the text for discussion of systematic uncertainties. "−5" indicates magnitude given is 5σ upper limit.
[e] Redshift source (in priority order if more than one redshifts exists): 1 = DEEP3 (Cooper et al. 2011, 2012), 2 = DEEP2 (Davis et al. 2003; Newman et al. 2012, http://deep.berkeley.edu/DR3/), 3 = MMT Hectospec (Coil et al. 2009), 4 = *Spitzer*/IRS (Huang et al. 2009; J.-S. Huang et al. (2012, in preparation), 5 = spectroscopic redshift from Rainbow (Barro et al. 2011a), 6 = photometric redshift from NMBS (Whitaker et al. 2011), 7 = photometric redshift from CFHTLS (Coupon et al. 2009: http://terapix.iap.fr/cplt/CFHTLS_deep_ugriz_T0004_zphot_1.4.tgz), 8 = photometric redshift from Huang et al. (2012), 9 = photometric redshift from Rainbow (Barro et al. 2011a).
[f] In W Hz^{-1}.

(This table is available in its entirety in a machine-readable form in the online journal. A portion is shown here for guidance regarding its form and content.)

4. DISCUSSION

4.1. Identification Rate

The overall identification rate of >99% is unprecedented for a radio sample of this size and depth, and the sensitive infrared data from IRAC were critical. Eighty-seven counterparts or 17% of the sample are fainter than the 90% catalog completeness limit of 21.08 mag. If the IRAC images had been shallower, then these sources would have been unidentified or incorrectly matched to neighboring sources brighter than the correct counterparts. Indeed, Afonso et al. (2011) achieved only 83% identification with their shallower IRAC data, though their radio sample (consisting solely of ultra-steep-spectrum radio sources) is not identical to ours and may preferentially include higher-redshift objects.

Spurious counterpart identifications from chance coincidence of radio sources with unrelated IRAC sources are unlikely. The IRAC source density (Barmby et al. 2008, Figure 9) at [3.6] < 21 is about 0.002 arcsec^{-2}. Thus, we would expect blind position matching of the whole radio sample with radius $0''7$ to produce less than one spurious match at this magnitude level. In fact, 417 counterparts have [3.6] < 21 (Figure 4), and position offsets are mostly $<0''7$ (Figure 1), consistent with expected position uncertainties. Of the fainter 93 sources, we expect ∼1 spurious match within $0''7$ and [3.6] < 23, but again the magnitudes are nearly all brighter and the position offsets smaller than these values. The most suspicious source is 033 with [3.6] = 22.4 and a position offset $1''3$. The proposed counterpart has a relatively flat SED (in F_ν, Table 5) from 3.6 to 8.0 μm, unusual for a normal galaxy but not for a radio source counterpart. Thus, we regard even a single spurious IRAC match for the simple radio sources as unlikely. The areal density of *R* < 26 sources is about five times higher than of [3.6] < 23 sources, and a few spurious matches at *R* cannot be ruled out. For the complex sources, the issue is not so much chance coincidences as uncertainty in the expected location of the counterpart relative to the radio emission. As discussed in

Table 5
IRAC Magnitudes

ID	Mag Type[a]	3.6 μm	±	4.5 μm	±	5.8 μm	±	8.0 μm	±
001	1	21.17	0.01	21.14	0.01	21.34	0.11	21.46	0.12
003	1	19.38	0.00	19.65	0.00	19.85	0.02	20.09	0.03
004	1	21.03	0.01	20.78	0.01	20.56	0.05	20.31	0.04
005	1	21.18	0.01	20.90	0.01	20.87	0.06	21.11	0.08
006	1	21.77	0.02	21.74	0.03	21.57	0.13	21.32	0.11

Notes. Data in AB magnitudes. Uncertainty is statistical only and is based on fluctuations in the nearby sky. It is shown as 0.00 when less than 0.005 mag, but see the text for discussion of systematic errors.
[a] Magnitude type: 1–3 = aperture magnitudes in $1''53$, $2''14$, or $3''06$ radii, respectively, 4 = magnitude in Kron aperture as measured by SExtractor.

(This table is available in its entirety in a machine-readable form in the online journal. A portion is shown here for guidance regarding its form and content.)

Section 2.1, alternate counterpart identifications are possible in some cases.

4.2. Nature of Sources

Radio emission can arise either from an AGN or from star formation (e.g., Rieke et al. 1980; Yun et al. 2001; Condon et al. 2002; Bell 2003; and especially Section 2.1 of Padovani et al. 2009 for comprehensive discussion). There are a variety of ways to separate the respective contributions (e.g., Padovani et al. 2009; Morić et al. 2010), but in general detailed followup at wavelengths other than radio and mid-infrared (MIR) is required.

For some objects, the source of emission is obvious. The low-redshift starburst population can be seen in Figure 6, where the 8 μm polycyclic aromatic hydrocarbon (PAH) emission makes low-*z* starbursts red in the [4.5]−[8.0] IRAC color (but does not affect [3.6]−[5.8], which remains blue) as long as $z \lesssim 0.5$. (See Figure 8 of Huang et al. 2007. Figure 2 of Padovani et al. 2011 is the equivalent diagram for their sample.) Figure 7 shows a
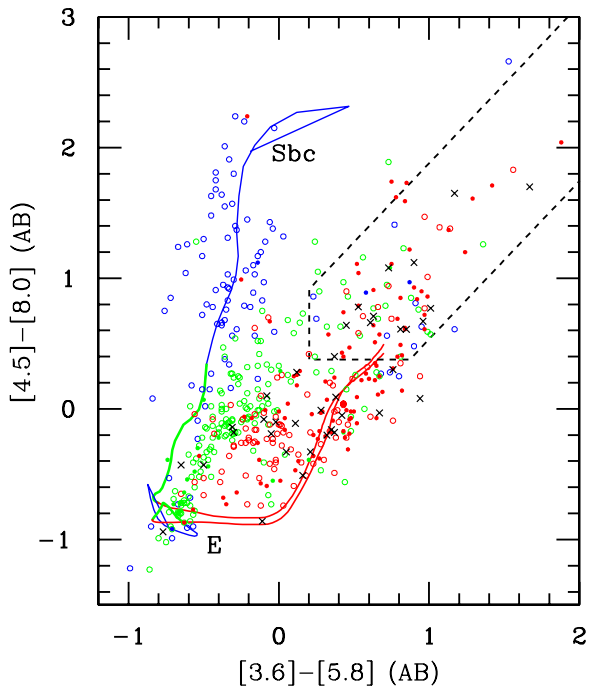
Figure 6. Color–color diagram for radio source counterparts showing the AGN selection region proposed by Donley et al. (2012). Circles denote objects with redshifts: blue for $z \leqslant 0.5$, green for $0.5 < z \leqslant 1.1$, and red for $z > 1.1$. Circles are filled if the radio luminosity $L(3\,\mathrm{GHz}) > 10^{23}$ W Hz^{-1} at $z \leqslant 0.5$ or $>10^{24}$ W Hz^{-1} at $z > 0.5$. Crosses denote objects lacking redshifts. Curves illustrate the colors of two template SEDs, one for an elliptical galaxy (E) and the other for an Sbc galaxy, as redshift increases from 0 to 4. The curves are color coded by redshift in the same way as the points and labeled near their respective $z = 0$ locations.

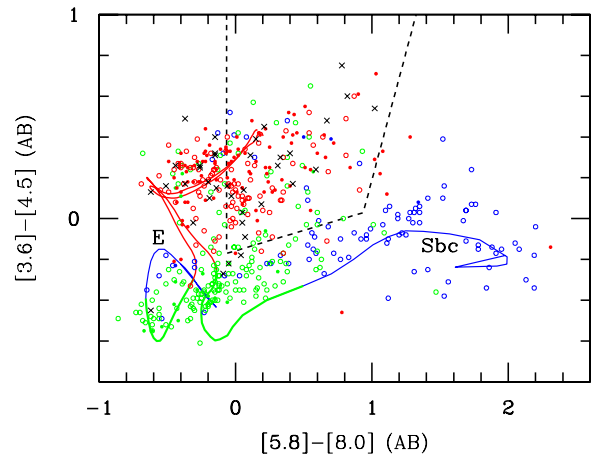(A color version of this figure is available in the online journal.)

Figure 7. Color–color diagram for radio source counterparts showing the AGN selection wedge proposed by Stern et al. (2005). Circles denote objects with redshifts: blue for $z \leqslant 0.5$, green for $0.5 < z \leqslant 1.1$, and red for $z > 1.1$. Circles are filled if the radio luminosity $L(3\,\mathrm{GHz}) > 10^{23}$ W Hz^{-1} at $z \leqslant 0.5$ or $>10^{24}$ W Hz^{-1} at $z > 0.5$. Crosses denote objects lacking redshifts. Curves illustrate the colors of two template SEDs, one for an elliptical galaxy (E) and the other for an Sbc galaxy, as redshift increases from 0 to 4. The curves are color coded by redshift in the same way as the points.

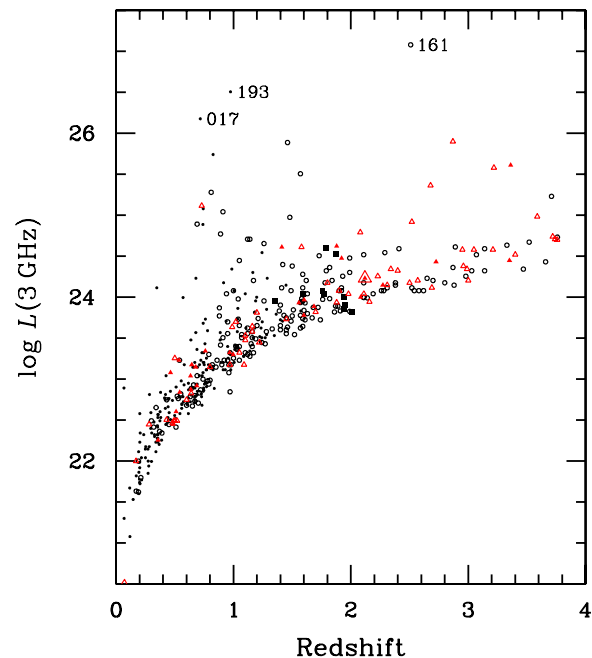(A color version of this figure is available in the online journal.)

different color–color plot. In both plots, the low-redshift galaxies are mostly within the starburst region, but a significant minority are in the AGN region. Depending on which color–color plot and the exact criteria one chooses, there are about 50–60 $z \leqslant 0.5$ galaxies in the low-z starburst category.

Other cases where the emission source is obvious are those with spectra that show strong PAH features. Huang et al. (2009) found 11 sources with $1.6 \leqslant z \leqslant 3.0$ and strong PAH features; seven of them are in the present radio sample. A seventh radio source in the Huang et al. list, not in their original sample but discovered serendipitously, shows no PAH features and is likely to be an AGN at $z = 2.12$ both from its spectrum and its MIR colors.

Radio power itself can be used as a criterion to separate star formation from active nuclei in local galaxies (e.g., Padovani et al. 2009), but it may not work well at large redshifts. A radio luminosity (measured for convenience at rest frequency 3 GHz) $L(3\,\mathrm{GHz}) = 10^{23}$ W Hz^{-1} corresponds to SFR = 100 $M_\odot$ yr^{-1} (Yun et al. 2001) for typical spectral index 0.7. Most local galaxies have SFR much lower than this. SFR = 200 $M_\odot$ yr^{-1} would correspond to $L(\mathrm{FIR}) > 10^{12} L_\odot$ (Kennicutt 1998), i.e., to a ULIRG, which are very rare locally. However, the ULIRG abundance is much higher at high redshift (e.g., Le Floc'h et al. 2005, Figure 14; Magnelli et al. 2011, Figure 9b), and the detection of 8234 $z \leqslant 1.2$ LIRGs in the COSMOS field (Feruglio et al. 2010) suggests that there could be of the order of 20 ULIRGs at $z < 1.2$ in the present sample. Figure 8 shows observed radio luminosities versus redshift for sample galaxies with known redshifts. At $z \leqslant 1.2$, there are 87 sample galaxies

Figure 8. Radio power as a function of redshift for all sources that have redshifts. Red triangles denote sources with MIR colors indicating AGN emission, and black circles denote other objects. Symbols are filled if the redshift is spectroscopic. Black squares denote ULIRG sources from (Huang et al. 2009; J.-S. Huang et al. 2012, in preparation), and the large red triangle denotes the one AGN source from Huang et al. (2009). Three extreme sources are labeled with source nicknames from Table 3.

(A color version of this figure is available in the online journal.)

with $L(3\,\mathrm{GHz}) > 2 \times 10^{23}$ W Hz^{-1}. Of these, 14 have $L(3\,\mathrm{GHz})$ an order of magnitude or more above this limit and are unlikely to be star forming, but the sheer numbers of such luminous galaxies also suggest that most are AGNs. The two objects with highest radio luminosity (at $z \leqslant 1.2$: 017 and 193) are radio doubles, clarifying the presence of an AGN at least in them. Overall redshifts, 27 sources have $L(3\,\mathrm{GHz}) > 5 \times 10^{24}$ W Hz^{-1},

above any known value for star formation (Chapman et al. 2010). The Huang et al. (2009) and J.-S. Huang et al. (2012, in preparation) sources should by selection be among the most luminous star formers, and their luminosities are all between 0.8 and 4×10^{24} W Hz^{-1}. It is therefore likely but not certain that the radio emission from the most luminous radio sources comes from an AGN, but radio luminosity alone is an uncertain criterion.

The MIR colors themselves can indicate the nature of the sources (Stern et al. 2005; Donley et al. 2012) but not with perfect reliability. For example, Barmby et al. (2006) found that half of their x-ray AGNs have MIR colors outside the Stern et al. (2005) AGN selection wedge. Donley et al. found almost 40% of powerful radio galaxies from the SHzRG sample (Seymour et al. 2007) outside their AGN selection region and fully 2/3 of $z > 1$ 3CRR radio galaxies (as distinguished from 3CRR quasars) outside it. Apparently some combination of obscuration of the MIR AGN emission by dust and veiling by the host galaxy can make the overall colors look like a normal or star-forming galaxy, especially if the host galaxy is luminous compared to the AGN. Worse, purely star-forming galaxy SEDs (at least as represented by some templates) can enter the Stern et al. (2005) AGN color–color region at some redshifts and for some values of dust reddening (Donley et al. 2012). The Donley et al. criteria were designed to avoid this contamination, but at the price of missing some AGNs. In the present sample, 97 objects (19%) have MIR colors in or very near the Donley et al. AGN box.[21] Park et al. (2010) found 31 of these to be power-law galaxies, which are clearly AGNs. (The Park et al. radio sample was the same one used in this paper.) Radio luminosities for the 83 objects with redshifts and AGN MIR colors range from 3×10^{20} to 8×10^{25} W Hz^{-1}, again showing that radio luminosity by itself is a poor criterion for source type.

The galaxies that lack redshifts have MIR colors consistent with AGN emission or high redshift or both. In Figure 7 in particular, almost all the galaxies without redshifts are either in the AGN wedge or just to its left where the $z > 1.5$ templates (and most of the 3CR radio galaxies) lie. This is confirmed more directly by Figure 9, which shows that the galaxies without redshifts almost all have $[3.6] - [4.5] > 0.1$. This color is consistent with $z \gtrsim 1.1$ or AGN emission or both. The objects without redshifts tend to be the faintest ones in the sample, as shown in Figure 5. This will make it difficult to obtain redshifts but is consistent with their being obscured AGNs or at $z >> 1$. Higdon et al. (2005) studied a sample of "optically invisible radio sources" (OIRSs) with $R \gtrsim 26.0$ and $I \gtrsim 25.6$. The surface density of such sources (Higdon et al. 2005) predicts more than 25 such objects in the present sample (which is slightly deeper in $S(1.4\,\mathrm{GHz})$ than the Higdon et al. sample), and in fact there are 46 objects with $R > 26$. Higdon et al. suggested that the vast majority (87%) of such sources are AGNs based on the lack of 24 μm detections, and Houck et al. (2005) gave evidence that even some OIRSs with 24 μm detections have spectra consistent with being powered by an AGN. Half of the OIRSs in the present sample have MIR colors outside the AGN boxes in Figures 6 and 7, and it seems likely that many of these are AGN-powered despite their MIR colors.

Even when the source of the radio emission is an AGN, the AGN emission need not dominate the rest-frame near-infrared
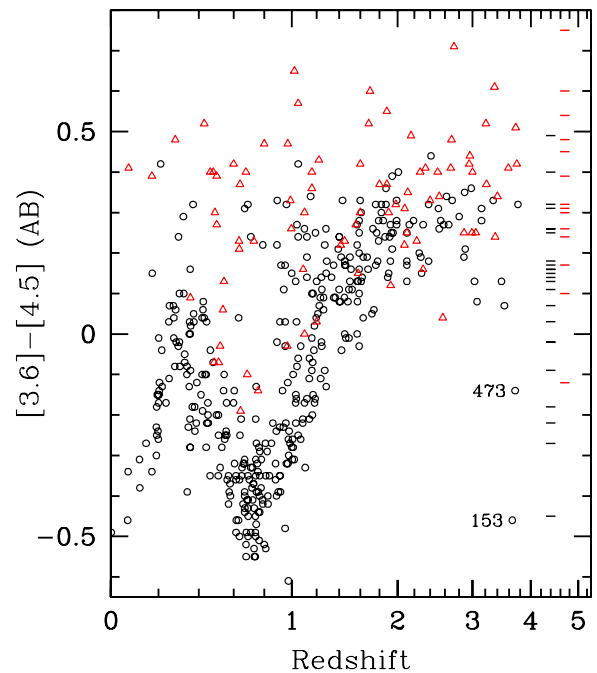

Figure 9. IRAC $[3.6] - [4.5]$ color vs. redshift (plotted as $\log(1 + z)$ for clarity). Red triangles denote objects with MIR colors indicating AGN emission, and black circles denote other sources. Colors of sources without redshifts are shown as dashes, plotted arbitrarily at redshift 4.7 for those with AGN colors and 4.4 for other objects. Two outliers are labeled with their source nicknames from Table 3.

(A color version of this figure is available in the online journal.)

emission. Figure 9 shows that for the majority of the sample, $[3.6] - [4.5]$ is consistent with a stellar population at the observed redshift. Figures 6 and 7 show many radio source counterparts inside the AGN regions but most outside. Thus, a substantial minority of radio source counterparts show AGN emission in the infrared, but most do not. The origin of the radio emission from these sources is unclear, and detailed followup will be needed to determine which galaxies are star forming and which are AGNs.

Authors studying other μJy radio samples have disagreed on the origin of the radio emission, although it has always been clear that AGNs and star-forming galaxies are both present (Benn et al. 1993). Barger et al. (2007) used visible spectroscopy and x-ray emission to separate star formers from AGNs and concluded that the majority of the $z < 1$ sample are star formers while at least 1/3 of the $L(3\,\mathrm{GHz}) > 2.6 \times 10^{23}$ W Hz^{-1} sample (mostly at $z > 1$) have x-ray luminosity characteristic of AGNs. A substantial allowance for x-ray obscured AGNs (e.g., Donley et al. 2005) must be added to the numbers of that last group. Chapman et al. (2010) detected far-infrared emission characteristic of star formation in at least 40 galaxies of a sub-sample of 68 radio sources above the same radio luminosity limit, but the requirement to have a spectroscopic redshift may have biased their sample against AGNs, and Morić et al. (2010) give reason for caution in interpreting FIR fluxes. Padovani et al. (2011) classified 63% of their radio source counterparts as AGNs based on a complex scheme involving a wide variety of data. They also found that the AGN fraction depends strongly on the radio flux density limit and on redshift.

All in all, about 10%–15% of the AEGIS20 sample consists of nearby star-forming galaxies, and about 20%–25% are AGNs, mostly at $z > 1$. The rest are a mix of types, but the exact

---

[21] Specifically, the count includes all objects with $[3.6] - [5.8] > 0.2$ and $[4.5] - [8.0] > 0.375$. Given their redshifts as indicated in Figure 6, the objects meeting these criteria are likely to be AGNs rather than star-forming contaminants.
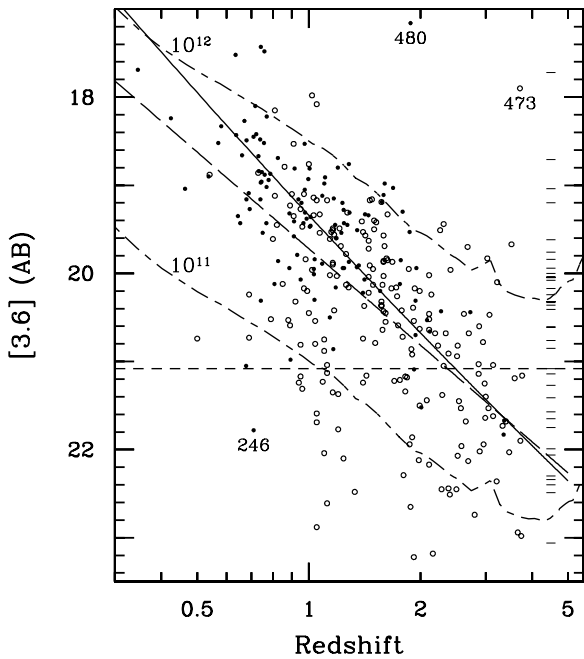
Figure 10. IRAC 3.6 μm magnitude as a function of redshift. Filled circles denote objects with spectroscopic redshifts, and open circles denote objects with photometric redshifts. Objects with $L(3\,\text{GHz}) < 10^{23}\,\text{W Hz}^{-1}$ are omitted; they are likely to be local starburst galaxies. Three outlying points are labeled with their source nicknames from Table 3. Magnitudes of objects with no redshift measurement are shown as dashes plotted at an arbitrary redshift of 4.5. The horizontal dashed line shows the 90% completeness limit of the IRAC catalog (Barmby et al. 2008). The solid curve shows the flux density from the K–z relation given by Willott et al. (2003), i.e., assuming constant flux density from observed 2.2 to 3.6 μm. The long-dashed line is the same, but using the Bryant et al. (2009) relation. The two short–long dashed lines show the flux density of instantaneous bursts of star formation occurring at $z = 6$ with initial masses 10^{11} and $10^{12}\,M_\odot$, respectively. (The actual stellar mass at relevant redshifts is 25%–30% less because of assumed mass loss.) The models come from Bruzual & Charlot (2003), use a Salpeter IMF, and include no dust extinction.

proportions are still unclear. Because the sample has essentially complete counterpart identification, it should be valuable in determining the origin of the radio emission and the fraction of obscured AGNs at high redshift. For comparison with other samples, the median redshift of the AEGIS20 sample is 1.03 (assuming the unmeasured redshifts are above this value). This is lower than that of the slightly deeper ($S_{1.4} > 43\,\mu$Jy) Mainieri et al. (2008) sample, which has a median redshift of 1.18 with 92% redshift completeness (Padovani et al. 2011). That degree of redshift completeness is vital; an earlier study (Padovani et al. 2009) of the Mainieri et al. sample with only 70% redshift completeness found a median redshift of 0.67.

4.3. The K–z Relation and Stellar Mass

Several studies (e.g., Willott et al. 2003; Rocca-Volmerange et al. 2004; Bryant et al. 2009) have noted a strong correlation between redshift and the observed 2.2 μm flux density. However, these studies have all involved samples with limiting radio flux densities $\gtrsim 200$ mJy. Figure 10 shows the 3.6 μm magnitude versus redshift for the current sample, for which few 2.2 μm (K) magnitudes are available. The wavelength difference between K and [3.6] will introduce a modest, redshift-dependent offset in the relation, but the basic form should not change because the dominant radiation source in both wavelengths is stars in the host galaxy. Indeed, Figure 10 shows that the [3.6]–z data are distributed around the known K–z relation but with large scatter.

The scatter is larger for sources with photometric redshifts but still substantial even for objects with spectroscopic redshifts. Using a synthetic K magnitude $K_{\text{synth}} \equiv [3.6] + a([3.6] - [4.5])$, where a is a constant of order unity, does not dramatically reduce the scatter. The two objects (233, 480) with [3.6] far brighter than the standard relation are likely to be QSOs, which are normally excluded from the K–z relation. The scatter is far too large to use the 3.6 μm magnitude as a way to determine redshift for individual objects, but as a group, the objects without measured redshifts have magnitudes consistent with $z > 1.1$.

The observed 3.6 μm magnitudes of the radio source counterparts give an indication of the stellar masses. At the redshifts of interest, radiation observed at 3.6 μm was emitted near the stellar radiation peak at 1.6 μm, and this is closely associated with the mass of the stellar population (e.g., Bell & de Jong 2001). Figure 10 shows the magnitudes that would be observed for single stellar populations that form instantaneously at $z = 6$ and evolve passively thereafter (Bruzual & Charlot 2003). Most of the radio source counterparts fall between the lines for 10^{11} and $10^{12}\,M_\odot$ but with substantial numbers below the $10^{11}\,M_\odot$ line. If the populations formed at $z < 6$, then the actual galaxy masses could be up to a factor of 3–5 smaller than indicated. Using Chabrier instead of Salpeter IMF would lower the masses by a factor of 1.7 (Bundy et al. 2006). Furthermore, some of the 3.6 μm light could come from an AGN rather than a stellar population; this is almost certainly the case for the extreme galaxies such as 480 and 473. On the other hand, the stellar population models do not include dust extinction, which could cause the masses to be underestimated by an unknown amount. Model fitting could give better mass estimates for individual galaxies, but the overall picture is that the radio sources live mostly in massive galaxies, but the range of stellar masses represented in the sample is larger than an order of magnitude.

5. CONCLUSIONS

IRAC images are a powerful means of identifying and classifying radio sources. Images with $\sim$9 ks IRAC depth giving $\sigma \approx 0.1\,\mu$Jy (Barmby et al. 2008) are sufficient to detect essentially all counterparts of radio sources in a sample with 1.4 GHz brightness limit of 50 μJy beam^{-1}. Radio sources at this depth are roughly 10%–15% local ($z \lesssim 0.5$) starbursts and 20%–25% AGNs, mostly at $z > 1$ with the remainder of uncertain nature. More than 1/3 of the sample have counterparts with $R_{\text{AB}} > 24$, and 15% have $R_{\text{AB}} > 25.5$. These sources would be very difficult to identify in R-band surveys, and if simple position matching were used, many would be incorrectly identified with brighter objects that are nearby on the sky but unrelated to the radio source.

The AEGIS20 sample, now essentially 100% identified, offers a great opportunity for detailed studies of the radio population. X-ray observations and additional spectra should enable a better classification between star-forming and active-nuclei galaxies, and the sample should yield luminosity functions and evolutionary history of the various populations.

REFERENCES

Afonso, J., Mobasher, B., Koekemoer, A., Norris, R. P., & Cram, L. 2006, AJ, 131, 1216
Afonso, J., Bizzocchi, L., Ibar, E., et al. 2011, ApJ, 743, 122
Bardelli, S., Schinnerer, E., Smolčic, V., et al. 2010, A&A, 511, A1
Barger, A. J., Cowie, L. L., & Wang, W.-H. 2007, ApJ, 654, 764
Barmby, P., Alonso-Herrero, A., Donley, J. L., et al. 2006, ApJ, 642, 126
Barmby, P., Huang, J.-S., Ashby, M. L. N., et al. 2008, ApJS, 177, 431
Barro, G., Pérez-González, P. G., Gallego, J., et al. 2011a, ApJS, 193, 13
Barro, G., Pérez-González, P. G., Gallego, J., et al. 2011b, ApJS, 193, 30
Bell, E. F. 2003, ApJ, 586, 794
Bell, E. F., & de Jong, R. S. 2001, ApJ, 550, 212
Benn, C. R., Rowan-Robinson, M., McMahon, R. G., Broadhurst, T. J., & Lawrence, A. 1993, MNRAS, 263, 98
Bertin, E., & Arnouts, S. 1996, A&AS, 117, 393
Bundy, K., Ellis, R. S., Conselice, C. J., et al. 2006, ApJ, 651, 120
Bruzual, G., & Charlot, S. 2003, MNRAS, 344, 1000
Bryant, J. J., Johnston, H. M., Broderick, J. W., et al. 2009, MNRAS, 395, 1099
Chapman, S. C., Ivison, R. J., Roseboom, I. G., et al. 2010, MNRAS, 409, L13
Ciliegi, P., Zamorani, G., Hasinger, G., et al. 2003, A&A, 398, 901

Coil, A. L., Georgakakis, A., Newman, J. A., et al. 2009, ApJ, 701, 1484
Condon, J. J., Cotton, W. D., & Broderick, J. J. 2002, AJ, 124, 675
Cooper, M. C., Aird, J. A., Coil, A. L., et al. 2011, ApJS, 193, 14
Cooper, M. C., Griffith, R. L., Newman, J. A., et al. 2012, MNRAS, 419, 3018
Coupon, J., Ilbert, O., Kilbinger, M., et al. 2009, A&A, 500, 981
Davis, M., Faber, S. M., Newman, J., et al. 2003, Proc. SPIE, 4834, 161
Davis, M., Guhathakurta, P., Konidaris, N. P., et al. 2007, ApJ, 660, L1
Donley, J. L., Rieke, G. H., Rigby, J. R., & Pérez-González, P. G. 2005, ApJ, 634, 169
Donley, J. L., Koekemoer, A. M., Brusa, M., et al. 2012, ApJ, 748, 142
Eisenhardt, P. R. M., Brodwin, M., Gonzalez, A. H., et al. 2008, ApJ, 684, 905
Feruglio, C., Aussel, H., Le Floc'h, E., et al. 2010, ApJ, 721, 607
Higdon, J. L., Higdon, S. J. U., Weedman, D. W., et al. 2005, ApJ, 626, 58
Houck, J. R., Soifer, B. T., Weedman, D., et al. 2005, ApJ, 622, L105
Huang, J.-S., Ashby, M. L. N., Barmby, P., et al. 2007, ApJ, 664, 840
Huang, J.-S., Faber, S. M., Daddi, E., et al. 2009, ApJ, 700, 183
Huang, J.-S., Faber, S. M., Willmer, C. N. A., et al. 2012, ApJ, submitted
Huynh, M. T., Jackson, C. A., Norris, R. P., & Fernandez-Soto, A. 2008, AJ, 135, 2470
Huynh, M. T., Norris, R. P., Siana, B., & Middelberg, E. 2010, ApJ, 710, 698
Ivison, R. J., Chapman, S. C., Faber, S. M., et al. 2007, ApJ, 660, L77
Kayser, R., Helbig, P., & Schramm, T. 1997, A&A, 318, 680
Kennicutt, R. C., Jr. 1998, ApJ, 498, 541
Le Floc'h, E., Papovich, C., Dole, H., et al. 2005, ApJ, 632, 169
Magnelli, B., Elbaz, D., Chary, R. R., et al. 2011, A&A, 528, A35
Mainieri, V., Kellermann, K. I., Fomalont, E. B., et al. 2008, ApJS, 179, 95
Morić, I., Smolčić, V., Kimball, A., et al. 2010, ApJ, 724, 779
Newman, J. A., Cooper, M. C., Davis, M., et al. 2012, ApJS, submitted (arXiv:1203.3192)
Padovani, P., Mainieri, V., Tozzi, P., et al. 2009, ApJ, 694, 235
Padovani, P., Miller, N., Kellermann, K. I., et al. 2011, ApJ, 740, 20
Park, S. Q., Barmby, P., Fazio, G. G., et al. 2008, ApJ, 678, 744
Park, S. Q., Barmby, P., Willner, S. P., et al. 2010, ApJ, 717, 1181
Rieke, G. H., Lebofsky, M. J., Thompson, R. I., Low, F. J., & Tokunaga, A. T. 1980, ApJ, 238, 24
Rocca-Volmerange, B., Le Borgne, D., De Breuck, C., Fioc, M., & Moy, E. 2004, A&A, 415, 931
Seymour, N., Stern, D., De Breuck, C., et al. 2007, ApJS, 171, 353
Simpson, C., Martnez-Sansigre, A., Rawlings, S., et al. 2006, MNRAS, 372, 741
Stern, D., Eisenhardt, P., Gorjian, V., et al. 2005, ApJ, 631, 163
Waddington, I., Windhorst, R. A., Dunlop, J. S., Koo, D. C., & Peacock, J. A. 2000, MNRAS, 317, 801
Whitaker, K. E., Labbé, I., van Dokkum, P. G., et al. 2011, ApJ, 735, 86
Willner, S. P., Coil, A. L., Goss, W. M., et al. 2006, AJ, 132, 2159
Willott, C. J., Rawlings, S., Jarvis, M. J., & Blundell, K. M. 2003, MNRAS, 339, 173
Yun, M. S., Reddy, N. A., & Condon, J. J. 2001, ApJ, 554, 803